Magnetotransport and angle-resolved photoemission spectroscopy of $MnSb_{12}Te_{19}$: a new member of $MnSb_{2n}Te_{3n+1}$ family

Mohit Mudgal,[1] Priyanka Meena,[1] Vishnu Kumar Tiwari,[1] Venkateswara Yenugonda,[1, 2] Vivek Kumar Malik,[3] Jens Buck,[4, 5] Kai Rossnagel,[4, 5] Sanjoy Kr Mahatha,[6] and Jayita Nayak[1, *]
[1]*Department of Physics, Indian Institute of Technology Kanpur, Kanpur 208016, India*
[2]*Department of Physics, SUNY Buffalo State University, Buffalo, NY- 14222, USA*
[3]*Department of Physics, Indian Institute of Technology Roorkee, Roorkee 247667, India*
[4]*Ruprecht Haensel Laboratory, Deutsches Elektronen-Synchrotron,*
DESY, Notkestr. 85, 22607 Hamburg, Germany
[5]*Institut für Experimentelle und Angewandte Physik,*
Christian-Albrechts-Universität zu Kiel, Olshausenstr. 40, 24098 Kiel, Germany
[6]*UGC-DAE Consortium for Scientific Research, Khandwa Road, Indore 452001, India*

The quest for intrinsically ferromagnetic topological materials is a focal point in the study of topological phases of matter, as intrinsic ferromagnetism plays a vital role in realizing exotic properties such as the anomalous Hall effect (AHE) in quasi-two-dimensional materials, and this stands out as one of the most pressing concerns within the field. Here, we investigate a novel higher order member of the $MnSb_{2n}Te_{3n+1}$ family, $MnSb_{12}Te_{19}$, for the first time combining magnetotransport and angle-resolved photoemission spectroscopy (ARPES) measurements. In $MnSb_{12}Te_{19}$, small hysteresis loop and large field saturation of the magnetization indicate weak ferromagnetism. Our magnetic susceptibility experiments identify ferromagnetic transitions at temperature $T_c = 18.7$ K, consistent with our heat capacity measurements (T=18.8 K). The AHE is observed for the field along the c-axis below T_c. Our study of Shubinikov-de-Haas (SdH) oscillations provides evidence for Dirac fermions with π Berry phase. Our comprehensive investigation reveals that $MnSb_{12}Te_{19}$ exhibits a weak FM ground state along with AHE, and hole-dominated transport properties consistent with ARPES measurements.

I. INTRODUCTION

The magnetic topological materials provide extraordinary opportunities not only for clarifying the exact relation between magnetism and nontrivial topological electronic states but also for discovering rich exotic unconventional topological quantum states such as the quantum anomalous Hall (QAH) insulators [1–3], axion insulators [4–6], and magnetic Weyl semimetals (WSMs) [7, 8]. Investigations into antiferromagnetic axion insulating phases have recently extended to compounds such as $MnBi_2Te_4$ and $MnBi_4Te_7$ [1, 9, 10]. In the $MnBi_4Te_7$ compound, magnetization-induced edge states are observed at the step edge of a magnetic $MnBi_2Te_4$ layer, while they are absent at nonmagnetic Bi_2Te_3 layers below the antiferromagnetic transition temperature $T_N =$ 12.5 K. These edge states disappear as the temperature surpasses T_N [11]. Additionally, Ding *et al.* reported from neutron diffraction experiments that an adequate fraction of Bi atoms occupy Mn sites in $MnBi_{2n}Te_{3n+1}$ (n=1, 2, 3, 4) compound, while Mn is not found at the non-magnetic atomic sites. Moreover, the occupancy of Mn monotonically decreases with the increase of n [12].

Utilizing density functional theory, Eremeev *et al.* proposed that $MnSb_{2n}Te_{3n+1}$ compounds might harbor multiple topologically nontrivial magnetic phases. According to their calculations, the ground states of the initial three members of this family (n = 1, 2, 3) are 3D antiferromagnetic topological insulators [13]. However, empirical findings contrast with this theoretical prediction, as demonstrated by $MnSb_2Te_4$ and $MnSb_4Te_7$, revealing versatile topological phases modulated by both carrier doping and magnetic field effects [14]. Particularly intriguing is the induction of superconductivity in the axion insulator $MnSb_4Te_7$ under pressure, which suppresses its antiferromagnetic order [15]. Meanwhile, the compound $MnBi_8Te_{13}$ showcases an intrinsic ferromagnetic axion insulating phase, unveiling a distinct half-magnetic state [4, 16]. Additionally, Zhang *et al.* reported strong magnetic competition in $MnSb_6Te_{10}$, realizing a fragile ferromagnetic ground state [17]. The study of $MnSb_8Te_{13}$ shows the weak ferromagnetism with dominating hole carriers. An anomaly near 5 T in the Hall data could be attributed to the Berry curvature-induced AHE. Electronic band structure calculations consistent with its ARPES measurements also confirmed the presence of an FM topological insulator phase in $MnSb_8Te_{13}$ [18]. $MnSb_{2n}Te_{3n+1}$ axion insulators are much less explored compared to their isostructural Bi compounds, that's why it is very important and exciting to study first time the electronic, physical, and magnetic properties of $MnSb_{12}Te_{19}$ to understand the underlying physics, which is not understood so far. However, to the best of our knowledge, no report is available on the $MnSb_{12}Te_{19}$ compound.

Here, we are first time reporting the magnetotransport properties along with the ARPES study of the new member of $MnX_{2n}Te_{3n+1}$ (X = Sb, Bi) family, with the highest order, i.e., $MnSb_{12}Te_{19}$. The comprehensive

---

[*] jnayak@iitk.ac.in

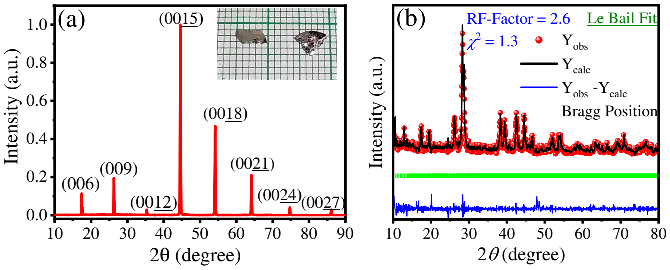

FIG. 1. (a) Single-crystal x-ray diffraction (XRD) results of $MnSb_{12}Te_{19}$ at 300 K. The inset shows the typical size of the single crystals. (b) Le Bail fit of the powder XRD of $MnSb_{12}Te_{19}$.

studies on the electronic and magnetotransport properties of $MnSb_{12}Te_{19}$ single crystals indicate the weak FM ground state along the c-axis. The Hall resistivity measurements reveal the anomalous Hall characteristic of the sample. ARPES measurements on the stoichiometric $MnSb_{12}Te_{19}$ single crystals reveal the valance band electronic structure near the Fermi energy and indicate the hole-dominated carriers consistent with our Hall resistivity calculations.

II. EXPERIMENTAL DETAILS AND METHODS

Using the self-flux method, we grew single crystals of $MnSb_{12}Te_{19}$. For the synthesis of $MnSb_{12}Te_{19}$ single crystals, the Mn (lumps, 99.95%, Alfa Aesar), Sb (shots, 99.999%, Alfa Aesar), and Te (lumps, 99.999%, Alfa Aesar) were weighted and mixed in the stoichiometry ratio. The mixture of materials was sealed inside a quartz tube under the one-third atmosphere of Ar. Then, the sample ampule was heated to 1000°C, stayed for 24 hours, and slowly cooled to 720°C for 24 hours. We cooled it further to 600°C for 48 hours before quenching the ampule in the ice water. The typical size of the plate-like crystals is $4.0\times4.0\times0.2$ mm^3, and the flat surface corresponds to the ab plane as shown in the inset of Figure 1(a). The grown crystals were characterized by X-ray diffraction (XRD) in a PANalytical X'Pert PRO diffractometer with Cu Kα_1 radiation and energy dispersion X-ray spectroscopy (EDS) measurements in a JEOL JSM-6010LA spectrometer to confirm the stoichiometry. To verify the composition more accurately, we have also performed the composition measurements using an electron probe micro-analyzer (EPMA) (Model: JXA-8230, JEOL), which gives the exact stoichiometry of the materials. We have conducted Le Bail fitting to determine the lattice parameters and crystal symmetry as shown in Figure 1(b). Using the standard four-probe technique, the electrical and magnetotransport measurements were carried out in a 12 T physical property measurement system (Quantum Design). Electrical contacts were made using a thin platinum wire and conducting silver paste. A sample rotator was used for the angle dependence of the MR between 0^0 and 360^0. ARPES measurements were carried out at the ASPHERE III end-station at beamline P04 of PETRA III, DESY. All the photoemission spectra were recorded at 90 K using a photon energy of 260 eV. The total energy and angular resolutions were better than 80 meV and 0.3°, respectively.

III. RESULTS AND DISCUSSIONS

A. Elemental analysis and Crystal structure

The elemental analysis was performed on flat surfaces cleaved in the air by EDS using two different techniques: tungsten-scanning electron microscopy (W-SEM) and EPMA. Multiple pieces from each batch were checked, and no composition variation was observed from the techniques. The measurements give a composition of Mn (3.25): Sb (36.69): Te (60.06) for the $MnSb_{12}Te_{19}$. The elemental analyses by different measurements suggest that $MnSb_{12}Te_{19}$ crystals are grown in perfect stoichiometry. The Mn concentration varies from 3 % to 3.25 % in the single crystals of $MnSb_{12}Te_{19}$. This could happen because the Mn site might host the extra Sb and create a little Mn vacancy. The crystallinity was examined using XRD measurements. The single crystal XRD of $MnSb_{12}Te_{19}$ is shown in Figure 1(a). Similar to the previous members of the family, $MnSb_{12}Te_{19}$ is crystallized in the $R-\bar{3}m$ (No. 166) space group, identified from phase matching by X'pert high score plus software and also confirmed by the Le Bail fit as shown in Figure 1(b). The Le Bail fitting of powder XRD data for $MnSb_{12}Te_{19}$, yielding a satisfactory fit with a χ^2 value of 1.3 and RF-factor of 2.6. The analysis indicates that the crystal structure is trigonal with a space group of $R-\bar{3}m$, grown in the c plane, similar to the other family members. The lattice parameters are as follows: $a = b = 4.3982$ Å, $c = 142.9895$ Å, and $\alpha = \beta = 90°$, and $\gamma = 120°$. These parameters are a solid foundation for more advanced Rietveld refinement, allowing for further fit optimization and deeper insights into the material's crystallographic properties.

From the EDS measurements with two different techniques, and Le Bail fit, we can firmly consider this sample as $MnSb_{12}Te_{19}$, the following member (n=6) of the family $MnSb_{2n}Te_{3n+1}$.

B. Magnetic measurements

The temperature-dependent magnetic susceptibility $\chi(T)$ in the zero-field cooling (ZFC) and field-cooling (FC) mode in the temperature range of 2 K to 300 K at $H = 100$ Oe along the out-of-plane ($H \parallel c$) direction has been measured as shown in Figure 2(a). Along the $H \parallel c$, the $\chi - T$ curve shows an FM transition at T_c = 18.7 K. The FM transition at 18.7 K is higher than

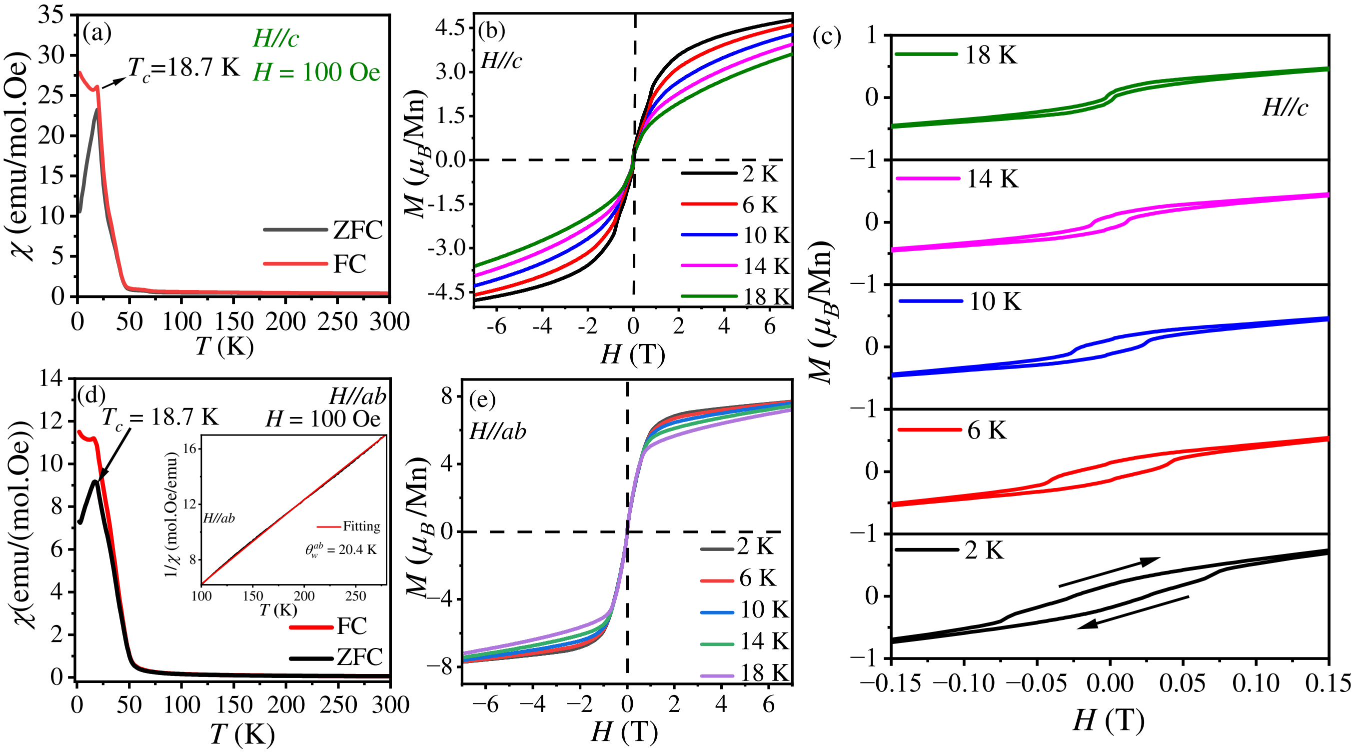

FIG. 2. (a) The temperature dependence of susceptibility χ at $H = 100$ Oe for $H \parallel c$. (b) The isothermal magnetization of $MnSb_{12}Te_{19}$ at various temperatures for $H \parallel c$ axis. (c) The hysteresis loop of isothermal magnetizations at various temperatures for $H \parallel c$ axis. (d) The temperature dependence of susceptibility χ at $H = 100$ Oe for $H \parallel ab$. (e) The isothermal magnetization at various temperatures for $H \parallel ab$ axis.

the other members of $MnSb_{2n}Te_{3n+1}$ (n=1, 2, 3, 4) family [14, 15, 17–19]. Thermal energy disrupts the aligned magnetic moments at elevated temperatures, causing the ferromagnetic properties to diminish beyond a specific critical temperature. The χ below 18.7 K for $H \parallel c$ exhibits a pronounced bifurcation, suggesting the formation of FM domains.

We have performed the field-dependent magnetization measurements at various temperatures to further investigate the magnetic properties of $MnSb_{12}Te_{19}$ single crystals. Figure 2(b) displays the isothermal magnetization with $H \parallel c$ at different temperatures. The hysteresis loops of isothermal magnetization demonstrate the ferromagnetic state as shown in Figure 2(c) at various temperatures for $H \parallel c$. The small hysteresis loop and large field saturation of the magnetization indicate weak ferromagnetism in the sample similar to the previously studied $MnSb_8Te_{13}$ [18].

The in-plane susceptibility also shows an FM transition at 18.7 K, as shown in Figure 2(d). The inset of Figure 2(d) shows the Curie-Weiss law fit of the reciprocal magnetic susceptibility ($1/\chi$) for $H \parallel ab$ between 100 K to 300 K measured with $H = 100$ Oe. The Weiss temperature for $MnSb_{12}Te_{19}$ is $\theta_w^{\mathrm{ab}} = 20.4$ K, near to the transition temperature in the susceptibility curve for $H \parallel c$. The effective magnetic moment is $\mu_{\mathrm{eff}} = 5.3\ \mu_B$/Mn, which is comparable to the magnetic moment of Mn^{+2}. Figure 2(e) displays the isothermal magnetization with $H \parallel ab$ at different temperatures. In $MnSb_{12}Te_{19}$, the saturation field for $H \parallel c$ is slightly smaller than that for $H \parallel ab$ at the same temperature, which indicates that the c-axis is the magnetic easy axis for $MnSb_{12}Te_{19}$, like the previous study of the $MnBi_8Te_{13}$ and $MnSb_8Te_{13}$ [4, 18]. This also indicates the magnetic anisotropy present in the sample, which occurs due to the strong spin-orbit coupling in magnetic TIs. The magnetic moment at a very low field is much less than the previous report of $MnSb_6Te_{10}$ [17] and $MnSb_4Te_7$ [15]. The reduced magnetic moment could be due to the Mn disorders and mixed location of Mn and Sb atoms [19]. The positive Weiss temperature indicates the FM ground state of $MnSb_{12}Te_{19}$ and is consistent with the previous study of $MnBi_8Te_{13}$ and $MnSb_8Te_{13}$ [4, 18].

C. Magnetotransport

The temperature dependence of longitudinal resistivity ρ_{xx} at $H = 0$ T for $I \parallel ab$ plane is presented in Figure 3(a). Beyond 20 K, the resistivity ρ_{xx} exhibits a nearly linear behavior that decreases with decreasing temperature. However, a slight increase is observed below 20 K,

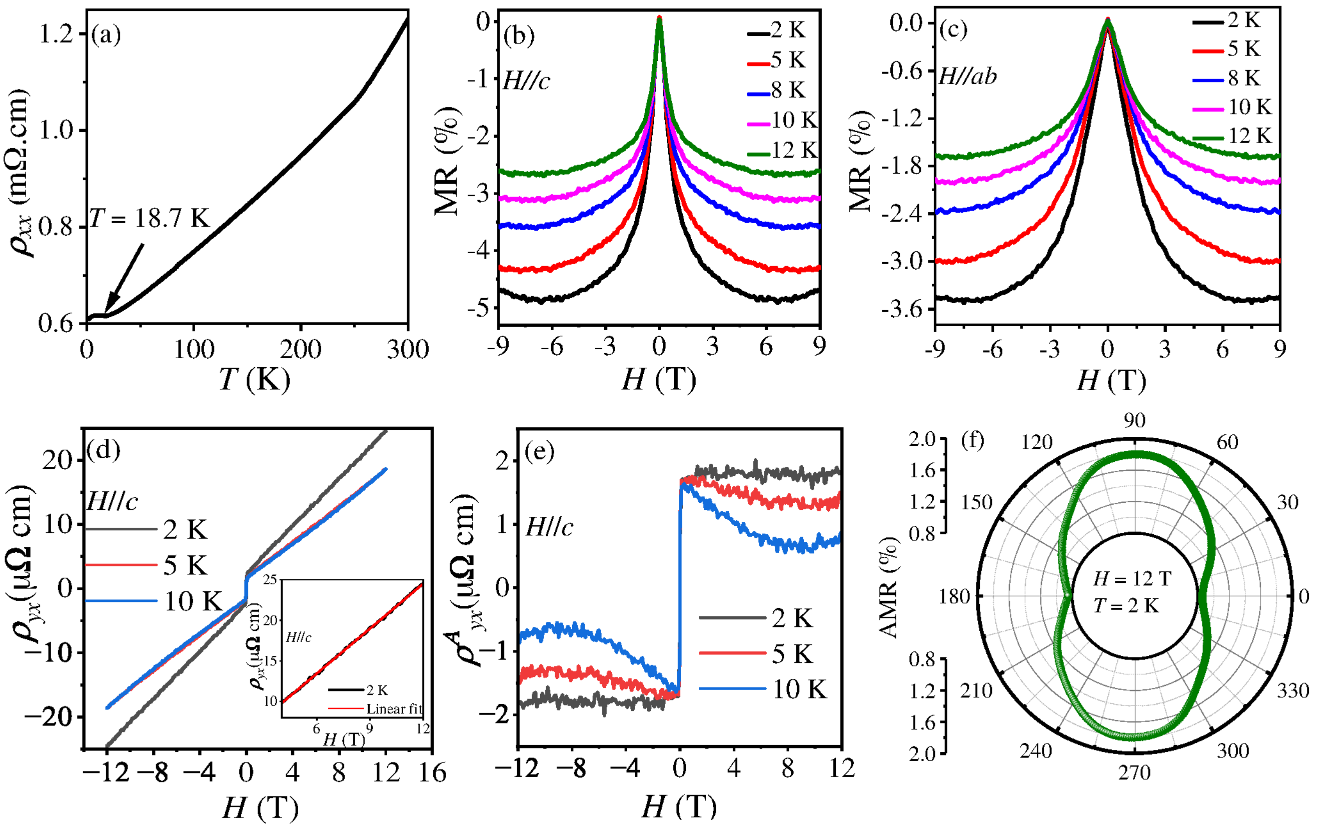

FIG. 3. (a) The temperature-dependent transverse resistivity ρ_{xx} at $H = 0$ T measured from 2 K to 300 K. The magnetic field dependence of (b) TMR ($H \parallel c$) and (c) LMR ($H \parallel ab$) of the $\mathrm{MnSb_{12}Te_{19}}$ crystal at different temperatures. (d) The magnetic field-dependent Hall resistivity at different temperatures for $H \parallel c$. The inset shows the linear fitting of Hall resistivity at 2 K. (e) The magnetic field-dependent anomalous Hall resistivity at different temperatures for $H \parallel c$. (f) Angle-dependent MR for $H \parallel c$ at $T = 2$ K and $H = 12$ T.

likely due to enhanced scattering from spin fluctuations, following a drop at 18.7 K, a common phenomenon in low-dimensional magnetic materials. The parallel alignment of Mn moments eliminates spin-slip scattering [18], thereby enhancing conductivity. The temperature dependence of the longitudinal resistivity has a residual resistance ratio $\rho(300\text{ K})/\rho(2\text{ K})$ of around 3, which indicates the possible presence of defects and disorders in the sample [18].

The magnetic field dependence of the transverse magnetoresistance (TMR) and longitudinal magnetoresistance (LMR) of $\mathrm{MnSb_{12}Te_{19}}$ at different temperatures has been shown in Figures 3(b) and 3(c), respectively. MR is calculated using the expression $\mathrm{MR} = (\rho_{xx}(H) - \rho_{xx}(0))/\rho_{xx}(0)$, where $\rho_{xx}(H)$ and $\rho_{xx}(0)$ are the resistivity in the presence and absence of the magnetic field, respectively. To eliminate the Hall resistivity contribution in MR, all the MR data has been symmetrized using the formula $\rho_{xx}(H) = [\rho_{xx}(+H) + \rho_{xx}(-H)]/2$.

In Figure 3(b), the negative TMR is the main feature for all measured temperatures. The significant negative TMR of about 5 % appears at 2 K for 9 T. Above 2 K, it remains negative till 12 K. The negative TMR feature can be understood in the framework of FM fluctuations [17, 18]. After cooling, FM fluctuations become increasingly stronger at low temperatures. As a result, the negative TMR arising from the FM fluctuations leads to a progressively deeper TMR shape upon cooling. In Figure 3(c), the negative LMR is largest with ~3.6 % at 2 K for 9 T. However, it decreases gradually with the increase in temperature and becomes ~1.8 % at 12 K for 9 T.

Figure 3(d) shows the measured data of experimental Hall resistivity. We have removed the MR contribution using the formula $\rho_{yx} = [\rho_{yx}(H) - \rho_{yx}(-H)]/2$. The Hall resistivity data shows linear field dependence at high temperatures. Below T_c, $\rho_{yx}(H)$ deviates from the linear dependence and shows a steep increase at low fields, signifying an anomalous Hall response. In general, the Hall resistivity in FM material has two parts: $\rho_{yx} = \rho^0_{yx} + \rho^A_{yx} = R_0 H + R_s M$, where ρ^0_{yx} and ρ^A_{yx} are the ordinary and anomalous Hall resistivity, respectively [20, 21]. R_0 is the ordinary Hall coefficient, and R_s is anomalous coefficient. The value of R_0 and R_s can be estimated from the linear fit of $\rho_{yx}(H)$ at a high field regime as shown in the inset of Figure 3(d), where the slope and the y-axis intercept corresponds to the R_0 and R_s, respectively. The anomalous Hall resistivity has been shown in Figure 3(e) for $H \parallel c$. The positive and linear behavior at the high field also indicates that the holes are the majority carriers in the sample. The carrier density n and Hall mobility μ have been estimated using the relations $n = 1/(eR_0)$ and $\mu = R_0/(\rho_{xx}(H = 0))$. The estimated carrier density is of the order of 10^{20} cm^{-3}, and the mobility is 27.10 $cm^2V^{-1}S^{-1}$ at 2 K, comparable to the previous study of $\mathrm{MnSb_8Te_{13}}$ [18].

The anisotropic character of the charge conduction mechanism linked to the electronic band structure can be investigated by resistivity measurements along various crystallographic orientations, but the size of the single crystals can restrict these measurements. In this situation, analyzing the direction-dependent TMR by rotating the magnetic field can provide some information on the nature of charge conduction in the sample [22]. Figure 3(f) shows AMR measured at 2 K and 12 T as a function of θ. The magnetic field is maintained along the rectangular crystal's out-of-plane (c-axis) direction. The rectangular crystal is slowly rotated about the magnetic field direction from the in-plane ($\theta = 0^o$) to the out-of-plane direction ($\theta = 90^o$). The MR reaches the maximum when the field is perpendicular to the crystal plane ($\theta \approx 0^o$) and the minimum when the field is along the plane ($\theta \approx 90^o$) as seen from Figure 3(f). These results probe the anisotropic nature of the charge conduction in the $\mathrm{MnSb_{12}Te_{19}}$.

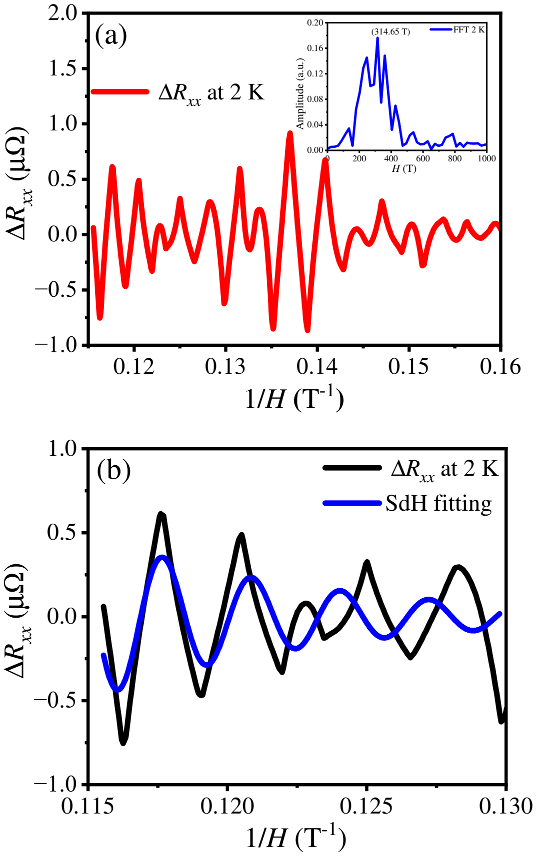

FIG. 4. (a) SdH oscillations with applied magnetic fields at 2 K and inset shows the FFT of the SdH oscillations at 2 K. (b) The SdH fitting of the oscillations at 2 K.

D. Shubinikov-de-Haas oscillations

Figure 4(a) displays the SdH oscillations with magnetic field dependence for $\mathrm{MnSb_{12}Te_{19}}$ at 2 K where the magnetic field is applied perpendicular to the basal plane of the crystal. Magnetoresistance curves are smoothed using a polynomial function to examine how the magnetic field affects $\mathrm{MnSb_{12}Te_{19}}$ resistance [23]. The detailed fluctuations are obtained by subtracting the actual signal's smoothed background, shown in Figure 4(a). FFT analysis of oscillations at 2 K shows that the frequency 314.65 T has the largest amplitude, as shown in the inset of Figure 4(a). Onsager relation was used to calculate the Fermi wave vectors for 2 K related to the prominent observed frequency of 314.65 T. The estimated Fermi wave vector K_F from the Onsager's relation $f_{SdH} = (\frac{\hbar}{2\pi e})\pi K_F^2$ is found to be $\sim$ 0.09792$\mathring{A}^{-1}$. The Fermi wave vector corresponding to the parabolic maxima in the ARPES plots of Figure 6(b) and 6(c) is $\sim$ 0.12032$\mathring{A}^{-1}$, near to the Fermi wave vector K_F at 2 K. To investigate the topological phase using the observed FFT frequency, i.e., whether they are trivial or non-trivial topological states, we have fitted the B dependence of the ΔR_{xx} with LK factor as shown in Figure 4(b). The LK relation can be written as [24–26],

$$\Delta R_{xx}(B) \propto cos[(\frac{f_{SdH}}{B} - \frac{1}{2} + \gamma)]e^{[-\alpha T_D/B]} \qquad (1)$$

Where f_{SdH} is the frequency of oscillations, B is the applied magnetic field, γ is the phase factor, T_D is Dingle temperature, and $\alpha = \frac{2\pi^2 k_B m^*}{\hbar e}$. The fitting of the LK factor yields the f_{SdH} (313.72 T) frequency comparable to the estimated from the FFT of the oscillations. The γ value is related to the Berry phase as $\gamma = \frac{\Phi_B}{2\pi}$, where ϕ_B is the Berry phase obtained by the carriers upon moving around the Dirac point. The calculated Berry phase is $\sim$ π, confirming the non-trivial nature of the Dirac fermions of the topological surface states [27]. We have also estimated the effective mass from equation 1 fitting, which comes out 0.28m_e, where m_e is the free electron mass. The related Fermi velocities, $v_F = \frac{\hbar K_F}{m^*}$, at 2 K is 4.05 × $10^5 ms^{-1}$. The fitting also provides the Dingle temperature, which can be used to calculate the carrier lifetime (τ). The estimated Dingle temperature is 35 K for the oscillations at 2 K. The calculated carrier lifetime from Dingle temperature ($T_D = \frac{\hbar}{2\pi k_B \tau}$) is 3.47 × 10^{-14} s for 2 K. The calculated mean free path $l_{SdH} = v_F\tau$ is 14.05 nm. The mobility μ_{SdH} $(=\frac{e\tau}{m^*})$ of the carriers is 217.89 $cm^2V^{-1}s^1$, which is one order higher than

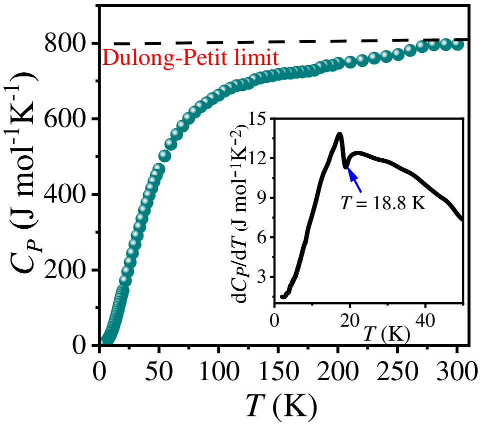

FIG. 5. Temperature dependence of the heat capacity of $MnSb_{12}Te_{19}$ at zero fields. The inset shows the temperature derivative of the heat capacity.

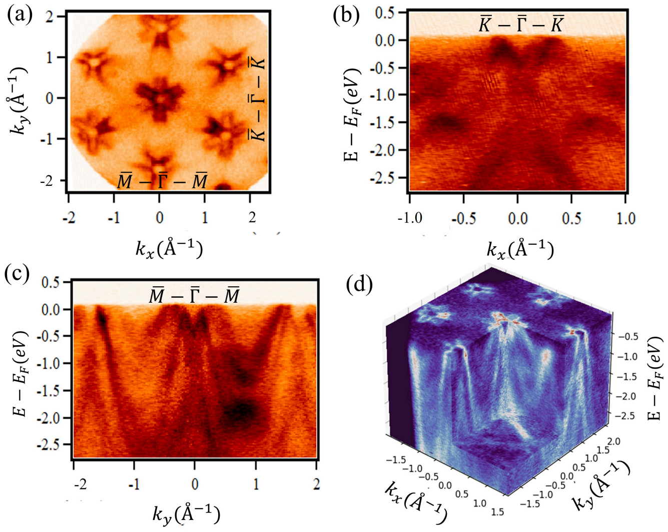

FIG. 6. (a) Isoenergy surface-map of the experimental ARPES spectrum at the Fermi level with incident photon energy, $h\nu = 260$ eV and temperature $T = 90$ K. (b-c) Experimentally measured electronic band dispersion along $\bar{K}-\bar{\Gamma}-\bar{K}$, and $\bar{M}-\bar{\Gamma}-\bar{M}$ high-symmetric directions as a function of the binding energy, respectively. (d) A three-dimensional view of the experimental valence band structure of $MnSb_{12}Te_{19}$ at 90 K.

the bulk carrier's mobility. The estimated surface carrier density at 2 K, n_s $(=\frac{\pi K_F^2}{(2\pi)^2})$ is 7.63×10^{12} cm^{-2}.

E. Heat capacity

The temperature dependence of the heat capacity (C_P) at constant pressure is shown in Figure 5(a). The signature of the transition at $T = 18.8$ K is visible in the temperature derivative of the heat capacity (see the inset of Figure 5(a)). The C_P increases continuously with the temperature and shows the saturation near the room temperature. The saturation value ($C_P = 796.28\, J\, mol^{-1}\, K^{-1}$) is almost equal to the limit set by the Dulong-Petit law ($C_P = 3nR = 797.76\, J\, mol^{-1}\, K^{-1}$, where n is the number of atoms in the formula units, and R is the universal gas constant).

F. Angle-resolved photoemission spectroscopy study of bulk $MnSb_{12}Te_{19}$

We have investigated the valence band electronic structure of layered $MnSb_{12}Te_{19}$ using soft x-ray ARPES experiments. In Fig. 6(a), we observe the experimental isoenergy surface map at the Fermi level, illustrating a six-fold rotational symmetry within the $k_x - k_y$ plane. This measurement was conducted at a photon energy of 260 eV and a temperature of 90 K. A feature of the three-dimensional valence bands close to the Fermi energy is the hexagonal patterns on the Fermi surface that vary in intensity throughout the $k_x - k_y$ plane. Interestingly, the Te-5p_z orbitals, which are hole-like, are primarily responsible for these hexagonal properties, while the electron-like Sb-5p_z orbitals contribute very little. Fig. 6(b-c) demonstrate ARPES intensity plot along $\bar{K} - \bar{\Gamma} - \bar{K}$, and $\bar{M} - \bar{\Gamma} - \bar{M}$ high-symmetric directions as a function of the binding energy, respectively. The experimental spectra closely resemble the bulk state continuum due to high photon energy and do not provide information about topological surface states near Fermi energy. These results revealed that $MnSb_{12}Te_{19}$ is a p-doped topological insulator, which explains the absence of band crossings near the Fermi level at the Γ-point consistent with the previous study of $MnSb_8Te_{13}$ [18]. 3D plot of the ARPES spectra has been depicted in Fig. 6(d) for better visualization of the bands.

IV. SUMMARY

In summary, we studied the physical properties of $MnSb_{12}Te_{19}$ single crystals with experimental measurements, including magnetic susceptibility, heat capacity, magnetoresistance, and the Hall effect, along with ARPES analysis. The magnetic susceptibility measurements showed the FM transition at $T_c = 18.7$ K for the fields perpendicular to the crystallographic c axis. The small hysteresis loop and large field saturation of the magnetization indicate weak ferromagnetism in the sample. We report the SdH oscillations in topological insulator $MnSb_{12}Te_{19}$. The SdH oscillations correspond to two important transport signatures: first, it provides evidence of the non-trivial nature of the bands with π-Berry phase, and second, the determined wave vector by FFT analysis is closely related to our ARPES results of the layered topological insulator $MnSb_{12}Te_{19}$. The heat capacity data follows the Dulong-Petit law limit. The electrical resistivity shows a change in the slope at the FM transition temperature of 18.7 K. The negative TMR strongly indicates the FM fluctuations along with the chiral anomaly effect, which needs to be confirmed in further studies. Hall resistivity data showed the AHE behavior with the single-band character of the compound and hole carrier domination, which is consistent with the ARPES measurements.

ACKNOWLEDGMENTS

We acknowledge IIT Kanpur and the Science and Engineering Research Board, India (project no: CRG/2023/007860, and SPG/2021/000443) for financial support. We acknowledge DESY (Hamburg, Germany), a member of the Helmholtz Association HGF, for providing experimental facilities. Parts of this research were carried out at PETRA III using beamline P04. Beamtime was allocated for proposal I-20221231. The photoemission spectroscopy instrument at beamline P04 was funded by the German Federal Ministry of Education and Research (BMBF) under the framework program ErUM (projects 05KS7FK2, 05K10FK1, 05K12FK1, 05K13FK1, 05K19FK4 with Kiel University; 05KS7WW1, 05K10WW2, and 05K19WW2 with the University of Würzburg). Financial support was approved by the Department of Science and Technology (Government of India) provided within the framework of the India@DESY collaboration is gratefully acknowledged.

---

[1] Y. Deng, Y. Yu, M. Z. Shi, Z. Guo, Z. Xu, J. Wang, X. H. Chen, and Y. Zhang, Quantum anomalous Hall effect in intrinsic magnetic topological insulator $MnBi_2Te_4$, Science **367**, 895 (2020).

[2] H. Deng, Z. Chen, A. Wołoś, M. Konczykowski, K. Sobczak, J. Sitnicka, I. V. Fedorchenko, J. Borysiuk, T. Heider, Ł. Pluciński, *et al.*, High-temperature quantum anomalous Hall regime in a $MnBi_2Te_4/Bi_2Te_3$ superlattice, Nature Physics **17**, 36 (2021).

[3] J. Li, Y. Li, S. Du, Z. Wang, B.-L. Gu, S.-C. Zhang, K. He, W. Duan, and Y. Xu, Intrinsic magnetic topological insulators in van der Waals layered $MnBi_2Te_4$-family materials, Science Advances **5**, eaaw5685 (2019).

[4] C. Hu, L. Ding, K. N. Gordon, B. Ghosh, H.-J. Tien, H. Li, A. G. Linn, S.-W. Lien, C.-Y. Huang, S. Mackey, J. Liu, P. V. S. Reddy, B. Singh, A. Agarwal, A. Bansil, M. Song, D. Li, S.-Y. Xu, H. Lin, H. Cao, T.-R. Chang, D. Dessau, and N. Ni, Realization of an intrinsic ferromagnetic topological state in $MnBi_8Te_{13}$, Science Advances **6**, eaba4275 (2020).

[5] M. M. Otrokov, I. P. Rusinov, M. Blanco-Rey, M. Hoffmann, A. Y. Vyazovskaya, S. V. Eremeev, A. Ernst, P. M. Echenique, A. Arnau, and E. V. Chulkov, Unique thickness-dependent properties of the van der Waals interlayer antiferromagnet $MnBi_2Te_4$ Films, Phys. Rev. Lett. **122**, 107202 (2019).

[6] J. Li, C. Wang, Z. Zhang, B.-L. Gu, W. Duan, and Y. Xu, Magnetically controllable topological quantum phase transitions in the antiferromagnetic topological insulator $MnBi_2Te_4$, Phys. Rev. B **100**, 121103 (2019).

[7] T. Suzuki, L. Savary, J.-P. Liu, J. W. Lynn, L. Balents, and J. G. Checkelsky, Singular angular magnetoresistance in a magnetic nodal semimetal, Science **365**, 377 (2019).

[8] J. Liu and L. Balents, Anomalous Hall effect and topological defects in antiferromagnetic Weyl semimetals: Mn_3Sn/Ge, Phys. Rev. Lett. **119**, 087202 (2017).

[9] M. M. Otrokov, I. I. Klimovskikh, H. Bentmann, D. Estyunin, A. Zeugner, Z. S. Aliev, S. Gaß, A. Wolter, A. Koroleva, A. M. Shikin, *et al.*, Prediction and observation of an antiferromagnetic topological insulator, Nature **576**, 416 (2019).

[10] C. Hu, K. N. Gordon, P. Liu, J. Liu, X. Zhou, P. Hao, D. Narayan, E. Emmanouilidou, H. Sun, Y. Liu, *et al.*, A van der Waals antiferromagnetic topological insulator with weak interlayer magnetic coupling, Nature communications **11**, 97 (2020).

[11] H.-K. Xu, M. Gu, F. Fei, Y.-S. Gu, D. Liu, Q.-Y. Yu, S.-S. Xue, X.-H. Ning, B. Chen, H. Xie, Z. Zhu, D. Guan, S. Wang, Y. Li, C. Liu, Q. Liu, F. Song, H. Zheng, and J. Jia, Observation of magnetism-induced topological edge state in antiferromagnetic topological insulator $MnBi_4Te_7$, ACS Nano **16**, 9810 (2022).

[12] L. Ding, C. Hu, E. Feng, C. Jiang, I. A. Kibalin, A. Gukasov, M. Chi, N. Ni, and H. Cao, Neutron diffraction study of magnetism in van der Waals layered $MnBi_{2n}Te_{3n+1}$, Journal of Physics D: Applied Physics **54**, 174003 (2021).

[13] S. V. Eremeev, I. P. Rusinov, Y. M. Koroteev, A. Y. Vyazovskaya, M. Hoffmann, P. M. Echenique, A. Ernst, M. M. Otrokov, and E. V. Chulkov, Topological magnetic materials of the $MnSb_2Te_4.(Sb_2Te_3)n$ van der Waals compounds family, The Journal of Physical Chemistry Letters **12**, 4268 (2021).

[14] S. Huan, S. Zhang, Z. Jiang, H. Su, H. Wang, X. Zhang, Y. Yang, Z. Liu, X. Wang, N. Yu, Z. Zou, D. Shen, J. Liu, and Y. Guo, Multiple magnetic topological phases in bulk van der Waals crystal $MnSb_4Te_7$, Phys. Rev. Lett. **126**, 246601 (2021).

[15] C. Pei, M. Xi, Q. Wang, W. Shi, J. Wu, L. Gao, Y. Zhao, S. Tian, W. Cao, C. Li, M. Zhang, S. Zhu, Y. Chen, H. Lei, and Y. Qi, Pressure-induced superconductivity in magnetic topological insulator candidate $MnSb_4Te_7$, Phys. Rev. Mater. **6**, L101801 (2022).

[16] R. Lu, H. Sun, S. Kumar, Y. Wang, M. Gu, M. Zeng, Y.-J. Hao, J. Li, J. Shao, X.-M. Ma, Z. Hao, K. Zhang, W. Mansuer, J. Mei, Y. Zhao, C. Liu, K. Deng, W. Huang, B. Shen, K. Shimada, E. F. Schwier, C. Liu, Q. Liu, and C. Chen, Half-magnetic topological insulator with magnetization-induced Dirac gap at a selected surface, Phys. Rev. X **11**, 011039 (2021).

[17] X. Zhang, S. Zhang, Z. Jiang, S. Huan, Y. Yang, Z. Liu, S. Yang, J. Jiao, W. Xia, X. Wang, N. Yu, Z. Zou, Y. Liu, J. Ma, D. Shen, J. Liu, and Y. Guo, Tunable

intrinsic ferromagnetic topological phases in a bulk van der Waals crystal $MnSb_6Te_{10}$ (2021), arXiv:2111.04973 [cond-mat.mtrl-sci].

[18] M. Mudgal, D. Dutta, P. Meena, V. Yenugonda, V. K. Tiwari, V. K. Malik, J. Buck, S. K. Mahatha, A. Agarwal, and J. Nayak, Magnetotransport and electronic structure of the axion insulator $MnSb_8Te_{13}$, Phys. Rev. B **110**, 045124 (2024).

[19] T. Murakami, Y. Nambu, T. Koretsune, G. Xiangyu, T. Yamamoto, C. M. Brown, and H. Kageyama, Realization of interlayer ferromagnetic interaction in $MnSb_2Te_4$ toward the magnetic Weyl semimetal state, Phys. Rev. B **100**, 195103 (2019).

[20] C.-Z. Chang, J. Zhang, X. Feng, J. Shen, Z. Zhang, M. Guo, K. Li, Y. Ou, P. Wei, L.-L. Wang, *et al.*, Experimental observation of the quantum anomalous Hall effect in a magnetic topological insulator, Science **340**, 167 (2013).

[21] G. Shi, M. Zhang, D. Yan, H. Feng, M. Yang, Y. Shi, and Y. Li, Anomalous Hall effect in layered ferrimagnet $MnSb_2Te_4$, Chinese Physics Letters **37**, 047301 (2020).

[22] A. Gupta, D. S. Kathyat, A. Mukherjee, A. Kumari, R. Tomar, Y. Singh, S. Kumar, and S. Chakraverty, Unique signatures of Rashba effect in angle-resolved magnetoresistance, Advanced Quantum Technologies **5**, 2100105 (2021).

[23] B. Bhattacharyya, A. Sharma, B. Sinha, K. Shah, S. Jejurikar, T. Senguttuvan, and S. Husale, Evidence of robust 2D transport and Efros-Shklovskii variable range hopping in disordered topological insulator (Bi_2Se_3) nanowires, Scientific reports **7**, 7825 (2017).

[24] P. Mal, B. Das, A. Lakhani, G. Bera, G. Turpu, J.-C. Wu, C. Tomy, and P. Das, Unusual conductance fluctuations and quantum oscillation in mesoscopic topological insulator $PbBi_4Te7$, Scientific Reports **9**, 7018 (2019).

[25] H. Cao, J. Tian, I. Miotkowski, T. Shen, J. Hu, S. Qiao, and Y. P. Chen, Quantized Hall effect and Shubnikov–de Haas oscillations in highly doped Bi_2Se_3: evidence for layered transport of bulk carriers, Phys. Rev. Lett. **108**, 216803 (2012).

[26] H. Murakawa, M. Bahramy, M. Tokunaga, Y. Kohama, C. Bell, Y. Kaneko, N. Nagaosa, H. Hwang, and Y. Tokura, Detection of Berry's phase in a bulk Rashba semiconductor, Science **342**, 1490 (2013).

[27] G. Mikitik and Y. V. Sharlai, Manifestation of Berry's phase in metal physics, Physical review letters **82**, 2147 (1999).